APPLIED PHYSICS

Electrically driven optical interferometry with spins in silicon carbide

Kevin C. Miao[1], Alexandre Bourassa[1], Christopher P. Anderson[1,2], Samuel J. Whiteley[1,2], Alexander L. Crook[1,2], Sam L. Bayliss[1], Gary Wolfowicz[1], Gergő Thiering[3], Péter Udvarhelyi[3,4], Viktor Ivády[3,5], Hiroshi Abe[6], Takeshi Ohshima[6], Ádám Gali[3,7], David D. Awschalom[1,2,8]*

Interfacing solid-state defect electron spins to other quantum systems is an ongoing challenge. The ground-state spin's weak coupling to its environment not only bestows excellent coherence properties but also limits desired drive fields. The excited-state orbitals of these electrons, however, can exhibit stronger coupling to phononic and electric fields. Here, we demonstrate electrically driven coherent quantum interference in the optical transition of single, basally oriented divacancies in commercially available 4H silicon carbide. By applying microwave frequency electric fields, we coherently drive the divacancy's excited-state orbitals and induce Landau-Zener-Stückelberg interference fringes in the resonant optical absorption spectrum. In addition, we find remarkably coherent optical and spin subsystems enabled by the basal divacancy's symmetry. These properties establish divacancies as strong candidates for quantum communication and hybrid system applications, where simultaneous control over optical and spin degrees of freedom is paramount.

INTRODUCTION

Solid-state spins have risen to prominence as qubits with atom-like properties combined with the fabrication advantages offered by the solid-state host. In particular, the neutral divacancy (VV) defect in silicon carbide (SiC) has attracted considerable attention for its near-infrared optical addressability (*1*), highly coherent spin (*2*), and adaptability stemming from SiC polytypism (*3*). Multiple methods of quantum control (*1*, *4*–*6*) have been demonstrated using the VV electron spin, while the SiC host material can be doped (*7*) and fabricated into nanostructures (*8*, *9*). Furthermore, *c* axis–oriented VVs have a high-fidelity spin-to-photon interface (*10*) and exhibit large dc Stark shifts under applied electric fields (*7*, *11*) and strain (*12*).

While the ground state of solid-state electron spins can be coherently controlled with acoustic (*5*, *13*, *14*) and electric (*4*) fields, the excited-state orbitals of these electrons can exhibit substantially larger acoustic (*12*, *15*, *16*) and electric (*7*, *11*, *17*, *18*) couplings, leading to enhanced interactions. In this work, we use the ground- and excited-state electronic orbital levels of single, basally oriented *kh* VVs in the 4H polytype of SiC to implement an optical two-level system (TLS). We demonstrate that this TLS, which has near–lifetime-limited coherence, can couple to electric fields, inducing a controllable σ_z (Pauli-Z) interaction in its Hamiltonian. This enables us to use ac electric fields to modulate the intensity and frequency profile of the *kh* VV resonant absorption spectrum between the levels of the TLS, inducing Landau-Zener-Stückelberg (LZS) interference fringes. Notably, the electric field coupling strength to the excited-state orbital is large enough that we observe classically driven coherent interactions with up to 15 microwave (MW) photons even in the absence of a MW resonator. We show that the coupling can be driven at a wide range of frequencies by demonstrating the TLS's complex spectral response under two simultaneous electric field drives at distinct frequencies. Last, we show that alongside the coherent optical interface, the *kh* VV's C_{1h} symmetry leads to a ground-state spin with long dephasing times and magnetically drivable spin rotations that span the eigenbasis. These results demonstrate extensive optical and spin control of *kh* VVs and pave the way for advanced quantum optics applications demanding high coherence across both photonic and spin subsystems.

RESULTS

We first outline the *kh* VV's physical configuration and associated orbital and spin energy levels. The *kh* VV defect in 4H-SiC consists of a carbon vacancy V_C adjacent to a silicon vacancy V_{Si} in the basally oriented *kh* configuration, where *k* and *h* refer to quasi-cubic and hexagonal local environments of the V_C and V_{Si} sites, respectively. Dangling bonds from the six neighboring atoms form a localized C_{1h} symmetry system, with a spin-1 orbital singlet ground state and orbital doublet excited state in the SiC electronic bandgap (Fig. 1, A and B). The resulting defect quantization axis is tilted at an angle of 71° with respect to the crystal *c* axis. At 5 K, where VV photoluminescence is typically the strongest, we take scanning confocal images of a 4H-SiC sample using 905-nm excitation (see Methods), revealing isolated emitters in the 10-μm wide gap of an on-chip capacitor (Fig. 1C). The emission spectrum of these isolated emitters shows about 10% of the emission in a zero-phonon line near 1079 nm, along with a red-shifted phonon sideband extending out to 1200 nm (Fig. 1A, inset), confirming the optical signature as *kh* VVs (*1*, *3*).

The C_{1h} symmetry manifests in the *kh* VV ground-state spin sublevels as longitudinal and transverse zero-field splittings D_{GS} and E_{GS}, producing spin eigenstates $\left\{|+\rangle = \frac{|+1\rangle+|-1\rangle}{\sqrt{2}}, |0\rangle, |-\rangle = \frac{|+1\rangle-|-1\rangle}{\sqrt{2}}\right\}$ in the $S_z = \{|+1\rangle, |0\rangle, |-1\rangle\}$ basis at low magnetic field (see Methods). We label this reduced symmetry spin triplet as ${}^3\tilde{A}_2$. Zero first-order Zeeman (ZEFOZ) transitions emerge (see Methods), suppressing magnetic field noise. In addition, magnetically driven

[1]Institute for Molecular Engineering, University of Chicago, Chicago, IL 60637, USA. [2]Department of Physics, University of Chicago, Chicago, IL 60637, USA. [3]Wigner Research Centre for Physics, Hungarian Academy of Sciences, PO Box 49, H-1525 Budapest, Hungary. [4]Department of Biological Physics, Loránd Eötvös University, Pázmány Péter sétány 1/A, H-1117 Budapest, Hungary. [5]Department of Physics, Chemistry and Biology, Linköping University, SE-581 83 Linköping, Sweden. [6]National Institutes for Quantum and Radiological Science and Technology, 1233 Watanuki, Takasaki, Gunma 370-1292, Japan. [7]Department of Atomic Physics, Budapest University of Technology and Economics, Budafoki út 8, H-1111 Budapest, Hungary. [8]Institute for Molecular Engineering and Materials Science Division, Argonne National Laboratory, Lemont, IL 60439, USA.
*Corresponding author. Email: awsch@uchicago.edu

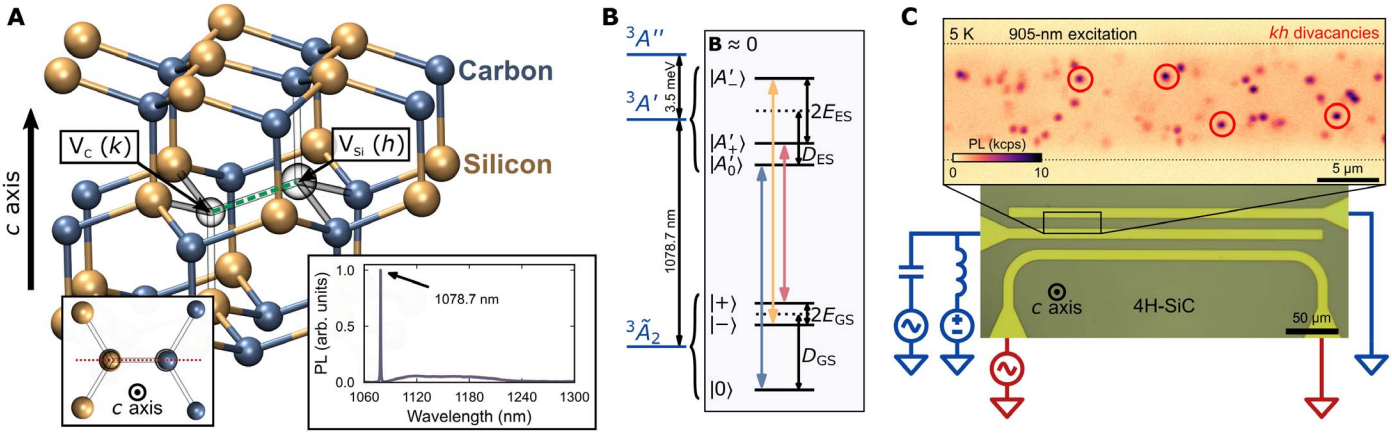

Fig. 1. Single *kh* VVs in commercially available 4H-SiC. (**A**) Lattice configuration of *kh* VVs in 4H-SiC. The defect axis is indicated by the green dashed line. Inset (left): Local atomic configuration around the *kh* VV showing C_{1h} symmetry. Inset (right): Emission spectrum of a single *kh* VV. arb. units, arbitrary units. (**B**) Energy diagram of the *kh* VV. The spin sublevels mix due to the effect of transverse zero-field splitting $E_{GS/ES}$, causing $|\pm1\rangle$ to become $|\pm\rangle$ near-zero external magnetic field. Spin-selective optical transitions (blue, yellow, and red arrows) enable spin-state readout. (**C**) Optical image of the 4H-SiC sample with a lithographically patterned capacitor and wire. Inset: Scanning confocal image of the marked region between the coplanar capacitor plates using 905-nm excitation. Highlighted emitters are single *kh* VVs. kcps, kilocounts per second.

spin transitions arise between $|0\rangle \leftrightarrow |\pm\rangle$ and $|+\rangle \leftrightarrow |-\rangle$, which we describe in detail later. In the excited state, the C_{1h} symmetry presents itself as a transverse crystal field, producing two widely separated $^3A'$ and $^3A''$ orbitals (Fig. 1B). We do not observe emission from $^3A''$ at 5 K, suggesting the presence of internal conversion causing fast relaxation from $^3A''$ to $^3A'$. Each orbital has three spin sublevels, and the fine structure of each orbital is also subject to longitudinal and transverse zero-field splittings D_{ES} and E_{ES}, which produce spin mixing similar to that in the ground state. Thus, we label the spin sublevels of $^3A'$ as $|A'_0\rangle$, $|A'_+\rangle$, $|A'_-\rangle$, analogous to $|0\rangle$, $|+\rangle$, $|-\rangle$ of $^3\tilde{A}_2$, respectively.

To map the fine structure of $^3A'$, we perform spin-dependent photoluminescence excitation (PLE) spectroscopy (see Methods) on a single *kh* VV in a charge-depleted environment, in which photoinduced charge dynamics of impurity sites are suppressed and spectral diffusion is reduced (*7*). We identify a central resonance corresponding to the $|0\rangle \leftrightarrow |A'_0\rangle$ transition, as well as two weaker detuned resonances primarily corresponding to $|+\rangle \leftrightarrow |A'_+\rangle$ and $|-\rangle \leftrightarrow |A'_-\rangle$ (Fig. 2A). From these resonance locations, we estimate the excited-state longitudinal and transverse excited-state zero-field splittings, D_{ES} and E_{ES}, to be +970 and −483 MHz, respectively. The notably large magnitude of E_{ES} suggests a significant change in electronic wave function distribution between the ground and excited state (see the Supplementary Materials). Furthermore, the spin selective nature of these transitions can be used for high-fidelity readout of the ground-state spin. While residual spectral diffusion of the optical transition frequency is observed (see the Supplementary Materials), we can sum over individual scans with the wandering compensated, allowing us to extract a 21.0(2)-MHz full width at half maximum of the Lorentzian line shape (Fig. 2A, inset).

We probe the excited-state dynamics of single *kh* VVs by performing time-correlated fluorescence measurements (see Methods). Optical excitation of $|0\rangle \leftrightarrow |A'_0\rangle$ and $|+\rangle \leftrightarrow |A'_+\rangle$ reveals coherent control of both transitions (Fig. 2B). A fit of the data to an integrated Bloch equation model reveals longitudinal and transverse relaxation times, as well as the spin relaxation rate under illumination (T_1, T_2, and Γ, respectively) (see Methods). On the time scale of the experiment, minimal spin relaxation under illumination for $|0\rangle \leftrightarrow |A'_0\rangle$ indicates that it may be cycling, while $|+\rangle \leftrightarrow |A'_+\rangle$ is noncycling and can be used for efficient spin pumping. For both transitions, the optical coherence T_2 approaches the lifetime limit of $2T_1$. We ascribe this to an exponential suppression of orbital mixing, given the large crystal field splitting, since the energy difference between the orbitals is expected to be larger than k_BT (where k_B is the Boltzmann constant). The near–lifetime-limited coherence of both optical transitions suggests that the spectral linewidth obtained through PLE spectroscopy may still be broadened by optical driving (*19*). Furthermore, the fidelity of coherent phenomena, such as interferometry and interaction gates in hybrid systems, benefits from long coherence times. In particular, the profile of the LZS interference spectrum depends on optical coherence time, which we show in detail later.

With the optical properties characterized, we can isolate a TLS in the energy structure and demonstrate LZS interference under an ac electric field drive. For our TLS, we use $|0\rangle \leftrightarrow |A'_0\rangle$ for its brightness and all-optical preparation sequence. LZS interference arises when the TLS is repeatedly brought through an avoided crossing diabatically, while a Stückelberg phase is acquired between each crossing (*20*). Optical driving of the TLS produces an avoided crossing, while the Stark effect allows for controlled passage through that crossing. According to the Landau-Zener formula, the diabatic transition probability through an avoided crossing of width Δ at a Landau-Zener velocity v is given by $P_{LZ} = e^{-\frac{2\pi\Delta}{4v}}$. We show that in our system, $v \gg \Delta$ is attainable, allowing us to operate in the diabatic regime. We couple highly confined electric fields between the on-chip planar capacitor plates (Fig. 1C) to single *kh* VVs, yielding dc Stark shifts of the VV's excited-state orbital levels that are resolvable through PLE spectroscopy (see the Supplementary Materials). We then apply a gigahertz-frequency ac electric field drive with zero dc bias concurrently with the resonant excitation. We monitor the PLE spectrum as we vary the amplitude $|\mathbf{F}|$ of a sinusoidal electric field drive with frequency $\omega = 2\pi \times 700$ MHz. At zero amplitude, only the bare resonance of $|0\rangle \leftrightarrow |A'_0\rangle$ is observed at zero laser detuning. With increasing amplitude, we produce multiphoton resonances at laser detunings equal to integer multiples of the drive frequency, culminating in classical

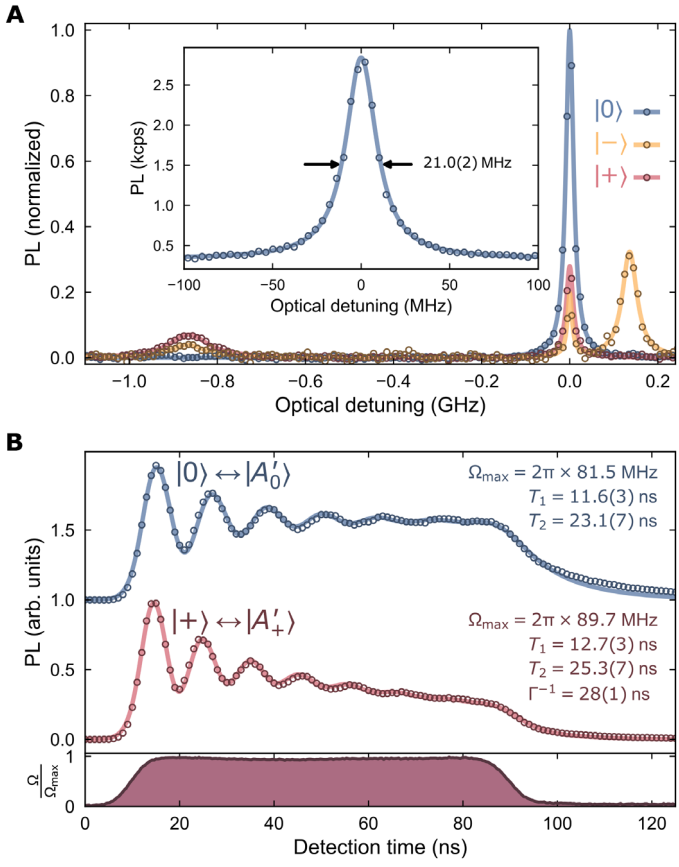

Fig. 2. Optical properties of single *kh* VVs. (**A**) PLE spectrum of a single *kh* VV prepared into $|0\rangle$ (blue), $|-\rangle$ (yellow), and $|+\rangle$ (red) with dc electric field (1 MV/m) applied and spectral diffusion compensated. Optical detuning measured with respect to 277.9337 THz (1078.647 nm). Inset: $|0\rangle \leftrightarrow |A_0'\rangle$ transition exhibiting a narrow, Lorentzian lineshape with spectral diffusion compensated. (**B**) Optical coherence of *kh* VVs. Optical Rabi oscillations between $|0\rangle \leftrightarrow |A_0'\rangle$ (blue circles) and $|+\rangle \leftrightarrow |A_+'\rangle$ (red circles) at 7.6-μW resonant excitation. Both transitions exhibit near–lifetime-limited optical coherence ($T_2 \approx 2\,T_1$). $|0\rangle \leftrightarrow |A_0'\rangle$ exhibits no detectable spin relaxation under illumination in this time scale, whereas excitation of $|+\rangle \leftrightarrow |A_+'\rangle$ rapidly depopulates $|+\rangle$. Bottom: The pulse envelope created by the acousto-optic modulator used to gate the resonant, narrow-line laser.

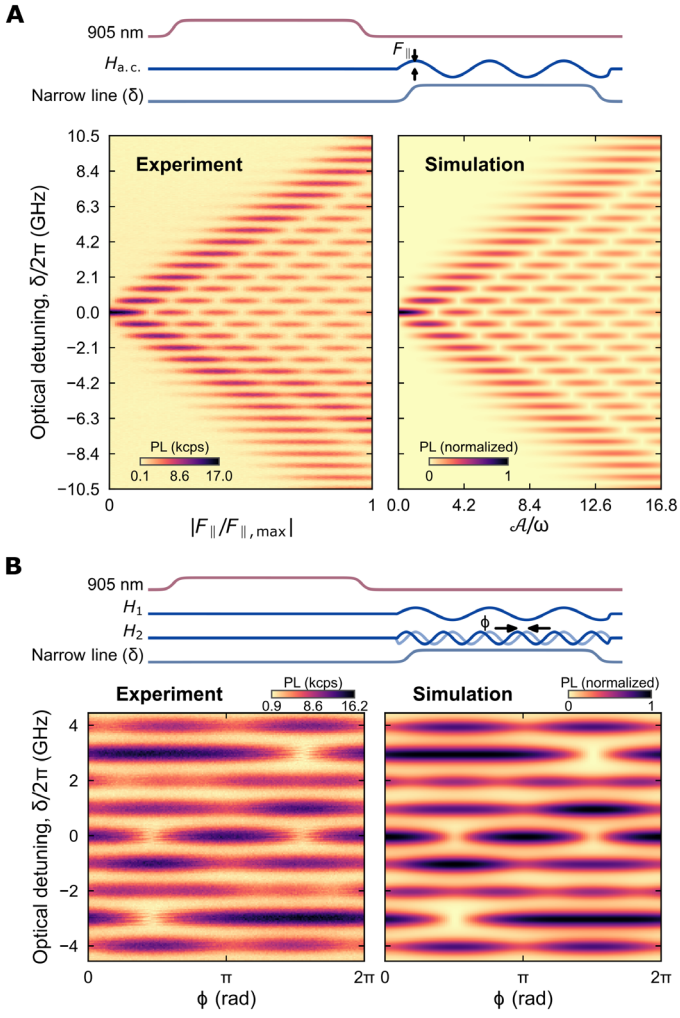

Fig. 3. LZS interferometry of *kh* VV absorption spectrum. (**A**) Monochromatic LZS interferometry of *kh* VV absorption spectrum. Top: Pulse sequence used to observe LZS interferometry. The interference pattern of $|0\rangle \leftrightarrow |A_0'\rangle$ is measured as a function of $\mathcal{A}$, the induced Stark shift amplitude. Bottom: Interference fringes of $|0\rangle \leftrightarrow |A_0'\rangle$ absorption arise in PLE spectroscopy as electric field magnitude $|\mathbf{F}|$ is increased ($|F_{\parallel,\max}| \approx 2$ MV/m), proportionally increasing $\mathcal{A}$. Total acquisition time was 19.5 hours. (**B**) Bichromatic LZS interferometry of *kh* VV absorption spectrum. Top: Pulse sequence used to observe bichromatic LZS interferometry. The interference pattern of $|0\rangle \leftrightarrow |A_0'\rangle$ is measured as a function of the relative phase ϕ of the two drives. Bottom: PLE of a single *kh* VV under two electric field drives ($\omega_1 = 2\pi \times 1$ GHz, $\omega_2 = 2\pi \times 2$ GHz, $\mathcal{A}_1/\omega_1 = \mathcal{A}_2/\omega_2 \approx 2.4048$) as a function of ϕ. Multiphoton resonances arise at $1 \times n$ GHz and $2 \times n$ GHz optical detunings, resulting in fringes from constructive and destructive interference of the two drives. Total acquisition time was 9.1 hours. kcps, kilocounts per second.

interactions with up to 15 MW photons when the laser is detuned by $\delta = 15 \times 2\pi \times 700$ MHz (Fig. 3A).

With the proper rotating frame transformations (see Methods), our observations can be explained by the Hamiltonian of the TLS in the rotating frame:

$$\frac{H''(t)}{\hbar} = \sum_{n=-\infty}^{\infty} \frac{\Delta_n}{2}\left(e^{-in\omega t}\sigma_+ + e^{in\omega t}\sigma_-\right) + \frac{\delta}{2}\sigma_z \qquad (1)$$

$$\Delta_n = \Omega J_n\left(\frac{\mathcal{A}}{\omega}\right)$$

$$\sigma_\pm = \frac{1}{2}\left(\sigma_x \pm i\sigma_y\right)$$

where δ is the optical detuning, Ω is the optical Rabi frequency, $J_n(x)$ are Bessel functions of the first kind, $\mathcal{A}$ is the amplitude of the induced Stark shift from the ac electric field, and ω is the ac electric field frequency. This Hamiltonian leads to LZS interference and multiphoton interactions where the bare optical resonance absorbs or emits quanta of energy resonant with the drive. In our system, Ω approaches $2\pi \times 200$ MHz, while $\mathcal{A}$ is swept up to $2\pi \times 11.76$ GHz. Since $\nu = \mathcal{A}\omega$ at the avoided crossing, we are in the diabatic regime for nearly all values of $\mathcal{A}$. Integrating the photoluminescence within the carrier resonance shows an approximate $|J_n(\frac{\mathcal{A}}{\omega})|$ dependence, which is expected in the strong optical driving regime, $T_1 T_2 \Omega^2 \gg 4\pi^2$ (see the Supplementary Materials). Together, these results demonstrate

coherent control of a single *kh* VV's orbital levels with MW frequency electric fields, which can enable a high-fidelity MW-to-optical interface when driven with single quanta of excitation.

We then turn our attention to bichromatic ac electric field driving enabled by the nonresonant capacitive structure. We apply drives $H_1 = \mathcal{A}_1\cos(\omega_1 t)\sigma_z$ and $H_2 = \mathcal{A}_2\cos(\omega_2 t + \phi)\sigma_z$, with amplitudes of both drives tuned to the first Bessel zero of the carrier resonance, $\mathcal{A}_1/\omega_1 = \mathcal{A}_2/\omega_2 \approx 2.4048$. We select two arbitrary, commensurable drive frequencies, $\omega_1 = 2\pi \times 1$ GHz and $\omega_2 = 2\pi \times 2$ GHz, both of which couple to the *kh* VV with similar strengths given the broadband nature of the capacitor (see the Supplementary Materials). The steady state of the TLS can then be described by higher-dimensional generalized Bessel functions (*21*). Specifically, the relative phase of the two drives can be tuned to break time reversal symmetry (*22*) and produce phase-dependent coherent destruction of tunneling. PLE spectroscopy taken while varying the relative phase ϕ reveals a phase-dependent structure well-matched to simulation (Fig. 3B), indicating coherent coupling to electric fields at two frequencies spanning an octave. These results suggest that temporal topological systems (*23*) can be simulated using polychromatic LZS phenomena in an electrically driven *kh* VV.

Last, we demonstrate the existence of a particularly versatile and coherent ground-state spin system in single *kh* VVs. At zero effective magnetic field (see Methods), $\mathbf{B}_{\text{eff}} = \vec{0}$, the mixed spin basis and resulting vanishing first derivative of the energy dispersion relation enable magnetically driven transitions between all three spin states and long spin dephasing times (Fig. 4A). We first show that the electron spin can span its eigenbasis by magnetically driving the $|0\rangle \leftrightarrow |+\rangle$ and $|+\rangle \leftrightarrow |-\rangle$ transitions at $D_{\text{GS}} + E_{\text{GS}} = 1.352373$ GHz and $2E_{\text{GS}} = 36.839$ MHz, respectively (see the Supplementary Materials). Using resonant spin-selective readout, we observe Rabi oscillations marked by high photoluminescence contrast (Fig. 4, B and C). We then perform Ramsey interferometry on single *kh* VVs prepared into $|\psi_0\rangle = \frac{1}{\sqrt{2}}(|0\rangle + |+\rangle)$ at the ZEFOZ point, revealing a ground-state spin dephasing time of $T_2^* = 74$ μs (Fig. 4D). Compared to *c* axis VVs, which have ground-state spin dephasing times around 2 μs (*24*), the lengthened spin dephasing time can be attributed to the suppression of first-order magnetic field sensitivity of the ZEFOZ point. Residual second-order magnetic field sensitivity and first-order electric field, however, may ultimately limit T_2^* (*25*, *26*). We use a Hahn-echo sequence to suppress higher-order magnetic field noise, allowing us to observe a spin coherence time of $T_2 = 222$ μs at the ZEFOZ point (Fig. 4E), comparable to low-field coherence times reported in *c* axis VVs (*2*). A Gaussian decay envelope suggests that bath ^{29}Si and ^{13}C nuclear spins are a main source of spin decoherence and that these contributions can be reduced by higher-order dynamical decoupling sequences such as XY-*n* (*27*).

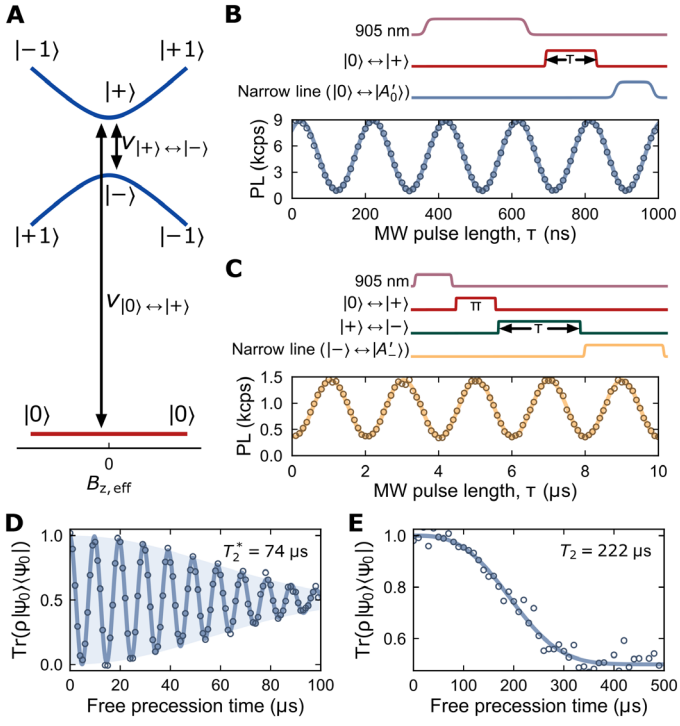

Fig. 4. Near-ZEFOZ spin control and dynamics of single *kh* VVs. (**A**) ZEFOZ transitions near zero effective magnetic field. Energy dispersion with respect to B_z shows the vanishing first derivative of the spin transition energies, $\nu_{|0\rangle \leftrightarrow |\pm\rangle}$ and $\nu_{|+\rangle \leftrightarrow |-\rangle}$, at $B_{z,\text{eff}} = 0$. (**B**) Top: Pulse sequence used to observe Rabi oscillations between $|0\rangle$ and $|+\rangle$. Bottom: Rabi oscillations of the ground-state spin between $|0\rangle$ and $|+\rangle$. PL measured from $|0\rangle \leftrightarrow |A_0'\rangle$ excitation. (**C**) Top: Pulse sequence used to observe Rabi oscillations between $|+\rangle$ and $|-\rangle$. Bottom: Rabi oscillations of ground-state spin between $|+\rangle$ and $|-\rangle$. PL measured from $|-\rangle \leftrightarrow |A_-'\rangle$ excitation. The nearby $|0\rangle \leftrightarrow |A_0'\rangle$ transition increases background and reduces the contrast of Rabi oscillations. (**D**) Ramsey interferometry of a spin superposition prepared in $|\psi_0\rangle = \frac{1}{\sqrt{2}}(|0\rangle + |+\rangle)$. Dephasing mechanisms evolve the initial state $\rho(0) = |\psi_0\rangle\langle\psi_0|$ into $\rho(t)$. A MW detuning of +100 kHz is added to increase visibility of the decay envelope. Readout is performed using $|0\rangle \leftrightarrow |A_0'\rangle$ PL. (**E**) Hahn-echo coherence of $|\psi_0\rangle = \frac{1}{\sqrt{2}}(|0\rangle + |+\rangle)$. A Gaussian decay envelope suggests the dominant source of spin decoherence is from the fluctuations of the ^{29}Si and ^{13}C nuclear spin bath.

DISCUSSION

Novel interactions between optical and MW photons in a solid-state system can be realized by leveraging the coherent coupling between electric fields and the excited-state orbitals of the *kh* VV. A bevy of MW resonator engineering techniques can allow adaptations to various applications using electric field coupling. For example, recent advances in high kinetic inductance superconducting resonators (*28*) can be leveraged to enhance zero-point fluctuations of the electric field. Consequently, protocols inspired by both atomic physics and circuit quantum electrodynamics can be explored, including the possibility of qubit-assisted resonator cooling where the optical transitions are driven in the resolved-sideband regime (*29*) and cavity-enhanced quantum-state readout (*30*). Furthermore, the relative ease of confining electric fields allows for independent interrogation of isolated, yet spatially proximal VVs, enabling a scalable architecture for multiqubit interactions (*31*). Meanwhile, remote entanglement applications requiring high Hong-Ou-Mandel interference visibility will benefit from the lifetime-limited coherence of the optical transitions (*32*). Collectively, these properties make *kh* VVs a versatile and promising platform to explore spin and optical dynamics coupled to an assortment of quantum control mechanisms.

METHODS

Sample preparation and experimental setup

We created samples from a 4″ commercially available wafer where 20 μm of high-purity i-type SiC ($[V_C]$,$[V_{Si}]$,$[N] < 1 \times 10^{15}$ cm^{-3}) was epitaxially grown on a 4° off-axis miscut of the Si face of a high-purity

semi-insulating SiC substrate (serial number A3177-14, Norstel AB). We diced 5 mm by 5 mm chips and performed electron irradiation with 2-MeV electrons at a dose of 3×10^{12} e^-/cm^2 to create both V_C and V_{Si}. Subsequent annealing at 850°C for 30 min in Ar formed VV complexes uniformly throughout the entire sample. Planar capacitors with a 10-μm gap width and wires with 10-μm width made of Ti/Au were then patterned on the sample surface using electron beam lithography. Samples were cooled to 5 K in a closed-cycle cryostat (Cryostation s100, Montana Instruments).

Using a confocal microscopy setup, we performed confocal raster scans using off-resonant excitation at 905 nm (QFLD-905-200S, QPhotonics) or 975 nm (BL975-SAG300, Thorlabs) focused through a microscope objective (LCPLN100XIR, Olympus). We detected emitted photons with >80% quantum efficiency using a low-jitter, low–dark count superconducting nanowire single-photon detector (SNSPD; Opus One, Quantum Opus). Electrical pulses from the SNSPD were converted to transistor-transistor logic and counted using a data acquisition module (PCI-6259, National Instruments). We applied a bandpass filter with a passband of 1064 to 1150 nm to selectively detect emission from *kh* divacancies while nearly completely rejecting emission from other defects and divacancy orientations. We performed PLE by scanning a narrow-line tunable laser (DL pro, TOPTICA Photonics) and collecting from the phonon sideband of the *kh* divacancies using a tunable longpass filter (TLP01-1116-25x36, Semrock). We initialized the spin with a pulse of off-resonant light, followed by spin manipulation using MW and radio frequency pulses. A pulse of resonant light performs spin-dependent readout. Spin driving with on-chip planar wires was achieved using a signal generator (SG396, Stanford Research Systems) modulated by an arbitrary waveform generator (for $|0\rangle \leftrightarrow |\pm\rangle$ transitions; AWG5014C, Tektronix) or an IQ modulator (for $|+\rangle \leftrightarrow |-\rangle$ transition; LTC5598, Analog Devices). LZS interferometry spectra were produced with MW frequency electric fields applied during the resonant readout pulse. We applied MWs generated in a similar fashion for spin driving across the on-chip capacitor, producing electric field magnitudes as high as 2 MV/m across the capacitor gap. Time-resolved photon arrival measurements were performed by time-tagging the SNSPD output pulses (Time Tagger 20, Swabian Instruments). We initialized the spin to $|0\rangle$ and performed MW rotations to prepare $|+\rangle$, followed by a laser pulse resonant with $|0\rangle \leftrightarrow |A_0^{'}\rangle$ or $|+\rangle \leftrightarrow |A_+^{'}\rangle$ for 80 ns. The arrival times of emitted photons in the phonon sideband were time-tagged relative to the start of the resonant laser pulse. Approximately five megacounts were collected over 60 min and histogrammed into 1-ns bins to observe time-resolved dynamics.

Spin Hamiltonian

The Hamiltonian of the divacancy ground state spin-1 system is

$$H/h = D\left(\hat{S}_z^2 - \frac{S(S+1)}{3}\right) + E(\hat{S}_+^2 + \hat{S}_-^2) + g\mu_B \mathbf{B}\cdot\hat{\mathbf{S}} + \sum_i \hat{\mathbf{S}}\cdot\mathbf{A}_i\cdot\hat{\mathbf{I}}_i \quad (2)$$

where D and E are the ground-state longitudinal and transverse zero-field splittings, respectively, μ_B is the Bohr magneton, g is the electron spin g factor, $\mathbf{B}$ is the external magnetic field, $\mathbf{A}_i$ is the hyperfine tensor of nuclear spin i, and $\hat{\mathbf{I}}_i$ is the nuclear spin operator vector of nuclear spin i. Zeeman interactions of the nuclear spin are neglected.

For simplicity, we would consider a system with one nuclear spin. Assuming B_x and B_y are negligible, diagonalization of this Hamiltonian yields the following eigenenergies

$$\mathrm{eigval}(H/h) = \begin{cases} D + \sqrt{C_+^2 + E^2}, & |1\rangle \\ D + \sqrt{C_-^2 + E^2}, & |2\rangle \\ D - \sqrt{C_+^2 + E^2}, & |3\rangle \\ D - \sqrt{C_-^2 + E^2}, & |4\rangle \\ 0, & |5\rangle \\ 0, & |6\rangle \end{cases} \quad (3)$$

and corresponding (unnormalized) eigenstates with a nuclear spin basis $I_z = \{|\uparrow\rangle, |\downarrow\rangle\}$

$$\mathrm{eigvec}(H/h) = \begin{cases} \frac{E}{C_+ + \sqrt{C_+^2 + E^2}}|+1\uparrow\rangle + |-1\uparrow\rangle, & |1\rangle \\ \frac{E}{C_- + \sqrt{C_-^2 + E^2}}|+1\downarrow\rangle + |-1\downarrow\rangle, & |2\rangle \\ \frac{E}{C_+ - \sqrt{C_+^2 + E^2}}|+1\uparrow\rangle + |-1\uparrow\rangle, & |3\rangle \\ \frac{E}{C_- - \sqrt{C_-^2 + E^2}}|+1\downarrow\rangle + |-1\downarrow\rangle, & |4\rangle \\ |0\uparrow\rangle, & |5\rangle \\ |0\downarrow\rangle, & |6\rangle \end{cases} \quad (4)$$

where $C_\pm = B_z \pm \frac{A_{zz}}{g\mu_B}$. When $C_\pm = 0$, the effect of B_z is to negate the hyperfine interaction for a particular nuclear spin orientation. For example, if we consider the system when the nuclear spin is $|\uparrow\rangle$ and $C_+ = 0$, then the electron spin Hamiltonian becomes equivalent to one with no nuclear spin interactions or external magnetic field, which allows us to label the effective external magnetic field as $B_{z,\mathrm{eff}} = B_z + \frac{A_{zz}}{g\mu_B} = 0$. At $C_+ = 0$ ($C_- = 0$), the first derivative of the energy difference ν between $|1\rangle$ ($|2\rangle$) and $|4\rangle$ ($|3\rangle$) as a function of B_z is zero, $\frac{d\nu}{dB_{z,\mathrm{eff}}} = 0$. Similar expressions can be derived for B_x and B_y, showing that $\frac{d\nu}{dB_{x,\mathrm{eff}}} = \frac{d\nu}{dB_{y,\mathrm{eff}}} = 0$ and that the field is $\mathbf{B}_{\mathrm{eff}} = 0$ to fulfill all these conditions. The vanishing first derivative of the energy dispersion, by definition, produces a ZEFOZ transition.

By operating at the ZEFOZ point, we selected one of the two nuclear spin states. The effective Hamiltonian can be expressed in the $S_z = \{|+1\rangle, |0\rangle, |-1\rangle\}$ basis

$$H_{\mathrm{ZEFOZ}}/h = \begin{bmatrix} D & 0 & E \\ 0 & 0 & 0 \\ E & 0 & D \end{bmatrix} \quad (5)$$

which can be diagonalized

$$H_{\mathrm{ZEFOZ}}^{'}/h = U^\dagger H_{\mathrm{ZEFOZ}} U/h = \begin{bmatrix} D+E & 0 & 0 \\ 0 & 0 & 0 \\ 0 & 0 & D-E \end{bmatrix} \quad (6)$$

$$U = \frac{1}{\sqrt{2}}\begin{bmatrix} 1 & 0 & 1 \\ 0 & \sqrt{2} & 0 \\ 1 & 0 & -1 \end{bmatrix}$$

where the eigenenergies of the three electron spin states are 0 and $D \pm E$, with corresponding eigenstates $|0\rangle$ and $\frac{1}{\sqrt{2}}(|+1\rangle \pm |-1\rangle)$. Spin-1 matrices in this basis can be expressed as

$$S_x' = \begin{bmatrix} 0 & 1 & 0 \\ 1 & 0 & 0 \\ 0 & 0 & 0 \end{bmatrix} S_y' = \begin{bmatrix} 0 & 0 & 0 \\ 0 & 0 & 1 \\ 0 & 1 & 0 \end{bmatrix} S_z' = \begin{bmatrix} 0 & 0 & 1 \\ 0 & 0 & 0 \\ 1 & 0 & 0 \end{bmatrix} \quad (7)$$

Thus, spin rotations can be achieved using the nonzero matrix elements (and their Hermitian conjugates) $\langle 0|S_x'|+\rangle$, $\langle 0|S_y'|-\rangle$, and $\langle -|S_z'|+\rangle$. Experimentally, we can realize S_x' and S_z' rotations, while S_y' rotations induce significant off-resonant S_x' rotation, given the defect orientation with respect to the planar drive wire.

LZS Hamiltonian

The Hamiltonian of the unperturbed optical transition can be considered as a TLS with a ground and excited state $|g\rangle = |0\rangle$ and $|e\rangle = |A_0'\rangle$, respectively. In the $\sigma_z = |e\rangle\langle e| - |g\rangle\langle g|$ basis, this Hamiltonian can be expressed as

$$H(t)/\hbar = \frac{\Omega \cos(\omega_{opt} t)}{2}\sigma_x + \frac{\omega_0}{2}\sigma_z \quad (8)$$

where Ω is the optical Rabi frequency, ω_{opt} is the laser frequency, and ω_0 is the optical resonance frequency. In the rotating frame of the TLS, a time-independent Hamiltonian arises

$$\tilde{H}/\hbar = \frac{\Omega}{2}\sigma_x + \frac{\delta}{2}\sigma_z \quad (9)$$

where $\delta = \omega_{opt} - \omega_0$ is the laser detuning from the resonance frequency. This system is analogous to the unperturbed TLS presented by Shevchenko *et al.* (*33*), with the substitutions $\Delta \rightarrow -\Omega$ and $\varepsilon \rightarrow -\delta$.

The addition of a longitudinally coupled ac electric field drive of amplitude $\mathcal{A}$ and frequency ω corresponds to an additional time-dependent Hamiltonian

$$H_{ac}(t)/\hbar = \frac{\mathcal{A}\cos(\omega t)}{2}\sigma_z \quad (10)$$

so that

$$\tilde{H}'(t)/\hbar = \frac{\tilde{H} + H_{ac}(t)}{\hbar} = \frac{\Omega}{2}\sigma_x + \frac{\delta + \mathcal{A}\cos(\omega t)}{2}\sigma_z \quad (11)$$

Applying a transformation (*33*) into a frame rotating with $H_{ac}(t)$ to $\tilde{H}(t)$ yields

$$\tilde{H}''(t)/\hbar = \frac{\delta}{2}\sigma_z + \sum_{n=-\infty}^{\infty} \frac{\Delta_n}{2}(e^{-in\omega t}\sigma_+ + e^{in\omega t}\sigma_-) \quad (12)$$

where $\Delta_n = \Omega J_n\left(\frac{\mathcal{A}}{\omega}\right)$ is the effective optical Rabi frequency under ac electrical drive.

Optical Bloch equation model

We modeled the *kh* divacancy optical structure as a three-level system in the presence of spin relaxation under illumination. In addition to the ground and excited states $|g\rangle$ and $|e\rangle$, we also considered a trapping state $|s\rangle$ representing noninteracting ground-state spin states. Furthermore, we introduced three relaxation channels in the form of Lindblad operators C_n: radiative decay, $C_1 = \frac{1}{\sqrt{T_1}}|g\rangle\langle e|$; pure dephasing, $C_2 = \frac{1}{\sqrt{T_2^*}}(|e\rangle\langle e| - |g\rangle\langle g|)$; and spin relaxation under illumination, $C_3 = \sqrt{\Gamma}|s\rangle\langle e|$. Our Hamiltonian takes the form

$$H(t)/\hbar = \frac{\Omega(t)}{2}(|g\rangle\langle e| + |e\rangle\langle g|) + \delta|e\rangle\langle e| \quad (13)$$

We then used mesolve provided by the QuTiP Python package, which solves the Lindblad master equation

$$\dot{\rho}(t) = -\frac{i}{\hbar}[H(t), \rho(t)] + \frac{1}{2}\sum_n \left(2C_n \rho C_n^\dagger - \{C_n^\dagger C_n, \rho\}\right) \quad (14)$$

where ρ is the density matrix, $[A, B] = AB - BA$ and $\{A, B\} = AB + BA$. Fitting to the data allows us to extract T_1, $T_2 = \left((2T_1)^{-1} + T_2^{*-1}\right)^{-1}$, and Γ^{-1}.

Density functional theory methodology

We used a plane wave basis set and projector augmented wave atomic potentials as implemented in Vienna Ab initio Simulation Package (VASP). The 4H-SiC supercell includes 576 atoms and embeds a single *hh* or *kh* divacancy. We used two exchange correlation functionals in our calculations, either the semilocal PBE functional or the HSE06 hybrid functional. The calculations were performed with a 420-eV plane wave cutoff energy using Γ-point sampling of the Brillouin zone. The excited-state electronic structure and geometry were calculated by constraint occupation of states. The splitting between the excited-state branches was determined from the splitting of the Kohn-Sham energies of the a' and a'' single-particle states in a $a_{a1}'(1)a_e'(1.5)a_e''(1.5)$ single-particle configuration. The relaxation path between the $^3A''$ and the $^3A'$ states was determined by nudged elastic band calculations. To calculate the permanent polarization of states, we used the VASP implementation of the Berry phase theory of polarization.

SUPPLEMENTARY MATERIALS

Supplementary material for this article is available at http://advances.sciencemag.org/cgi/content/full/5/11/eaay0527/DC1

REFERENCES AND NOTES

1. W. F. Koehl, B. B. Buckley, F. J. Heremans, G. Calusine, D. D. Awschalom, Room temperature coherent control of defect spin qubits in silicon carbide. *Nature* **479**, 84–87 (2011).
2. H. Seo, A. L. Falk, P. V. Klimov, K. C. Miao, G. Galli, D. D. Awschalom, Quantum decoherence dynamics of divacancy spins in silicon carbide. *Nat. Commun.* **7**, 12935 (2016).
3. A. L. Falk, B. B. Buckley, G. Calusine, W. F. Koehl, V. V. Dobrovitski, A. Politi, C. A. Zorman, P. X. Feng, D. D. Awschalom, Polytype control of spin qubits in silicon carbide. *Nat. Commun.* **4**, 1819 (2013).
4. P. V. Klimov, A. L. Falk, B. B. Buckley, D. D. Awschalom, Electrically driven spin resonance in silicon carbide color centers. *Phys. Rev. Lett.* **112**, 087601 (2014).
5. S. J. Whiteley, G. Wolfowicz, C. P. Anderson, A. Bourassa, H. Ma, M. Ye, G. Koolstra, K. J. Satzinger, M. V. Holt, F. J. Heremans, A. N. Cleland, D. I. Schuster, G. Galli, D. D. Awschalom, Spin-phonon interactions in silicon carbide addressed by Gaussian acoustics. *Nat. Phys.* **15**, 490–495 (2019).
6. F. J. Heremans, C. G. Yale, D. D. Awschalom, Control of spin defects in wide-bandgap semiconductors for quantum technologies. *Proc. IEEE* **104**, 2009–2023 (2016).
7. C. P. Anderson, A. Bourasssa, K. C. Miao, G. Wolfowicz, P. J. Mintun, A. L. Crook, H. Abe, J. U. Hassan, N. T. Son, T. Ohshima, D. D. Awschalom, Electrical and optical control of single spins integrated in scalable semiconductor devices. arXiv: 1906.08328 [quant-ph] (19 June 2019).
8. G. Calusine, A. Politi, D. D. Awschalom, Cavity-enhanced measurements of defect spins in silicon carbide. *Phys. Rev. Appl.* **6**, 014019 (2016).
9. D. O. Bracher, X. Zhang, E. L. Hu, Selective Purcell enhancement of two closely linked zero-phonon transitions of a silicon carbide color center. *Proc. Natl. Acad. Sci. U.S.A.* **114**, 4060–4065 (2017).
10. D. J. Christle, P. V. Klimov, C. F. de las Casas, K. Szász, V. Ivády, V. Jokubavicius, J. U. Hassan, M. Syväjärvi, W. F. Koehl, T. Ohshima, N. T. Son, E. Janzén, Á. Gali, D. D. Awschalom, Isolated spin qubits in sic with a high-fidelity infrared spin-to-photon interface. *Phys. Rev. X* **7**, 021046 (2017).
11. C. F. de las Casas, D. J. Christle, J. U. Hassan, T. Ohshima, N. T. Son, D. D. Awschalom, Stark tuning and electrical charge state control of single divacancies in silicon carbide. *Appl. Phys. Lett.* **111**, 262403 (2017).
12. A. L. Falk, P. V. Klimov, B. B. Buckley, V. Ivády, I. A. Abrikosov, G. Calusine, W. F. Koehl, Á. Gali, D. D. Awschalom, Electrically and mechanically tunable electron spins in silicon carbide color centers. *Phys. Rev. Lett.* **112**, 187601 (2014).
13. E. R. MacQuarrie, T. A. Gosavi, N. R. Jungwirth, S. A. Bhave, G. D. Fuchs, Mechanical spin control of nitrogen-vacancy centers in diamond. *Phys. Rev. Lett.* **111**, 227602 (2013).
14. J. Teissier, A. Barfuss, P. Appel, E. Neu, P. Maletinsky, Strain coupling of a nitrogen-vacancy center spin to a diamond mechanical oscillator. *Phys. Rev. Lett.* **113**, 020503 (2014).
15. D. A. Golter, T. Oo, M. Amezcua, K. A. Stewart, H. Wang, Optomechanical quantum control of a nitrogen-vacancy center in diamond. *Phys. Rev. Lett.* **116**, 143602 (2016).
16. H. Y. Chen, E. R. MacQuarrie, G. D. Fuchs, Orbital state manipulation of a diamond nitrogen-vacancy center using a mechanical resonator. *Phys. Rev. Lett.* **120**, 167401 (2018).
17. P. Tamarat, T. Gaebel, J. R. Rabeau, M. Khan, A. D. Greentree, H. Wilson, L. C. L. Hollenberg, S. Prawer, P. Hemmer, F. Jelezko, J. Wrachtrup, Stark shift control of single optical centers in diamond. *Phys. Rev. Lett.* **97**, 083002 (2006).
18. L. C. Bassett, F. J. Heremans, C. G. Yale, B. B. Buckley, D. D. Awschalom, Electrical tuning of single nitrogen-vacancy center optical transitions enhanced by photoinduced fields. *Phys. Rev. Lett.* **107**, 266403 (2011).
19. A. Batalov, C. Zierl, T. Gaebel, P. Neumann, I. Y. Chan, G. Balasubramanian, P. R. Hemmer, F. Jelezko, J. Wrachtrup, Temporal coherence of photons emitted by single nitrogen-vacancy defect centers in diamond using optical rabi-oscillations. *Phys. Rev. Lett.* **100**, 077401 (2008).
20. E. C. G. Stueckelberg, Theorie der unelastischen Stösse zwischen Atomen. *Helv. Phys. Acta* **5**, 369–422 (1932).
21. H. J. Korsch, A. Klumpp, D. Witthaut, On two-dimensional Bessel functions. *J. Phys. A Math. Gen.* **39**, 14947–14964 (2006).
22. F. Forster, M. Mühlbacher, R. Blattmann, D. Schuh, W. Wegscheider, S. Ludwig, S. Kohler, Landau-Zener interference at bichromatic driving. *Phys. Rev. B* **92**, 245422 (2015).
23. I. Martin, G. Refael, B. Halperin, Topological frequency conversion in strongly driven quantum systems. *Phys. Rev. X* **7**, 041008 (2017).
24. D. J. Christle, A. L. Falk, P. Andrich, P. V. Klimov, J. U. Hassan, N. T. Son, E. Janzén, T. Ohshima, D. D. Awschalom, Isolated electron spins in silicon carbide with millisecond coherence times. *Nat. Mater.* **14**, 160–163 (2014).
25. F. Dolde, H. Fedder, M. W. Doherty, T. Nöbauer, F. Rempp, G. Balasubramanian, T. Wolf, F. Reinhard, L. C. L. Hollenberg, F. Jelezko, J. Wrachtrup, Electric-field sensing using single diamond spins. *Nat. Phys.* **7**, 459–463 (2011).
26. P. Jamonneau, M. Lesik, J. P. Tetienne, I. Alvizu, L. Mayer, A. Dréau, S. Kosen, J.-F. Roch, S. Pezzagna, J. Meijer, T. Teraji, Y. Kubo, P. Bertet, J. R. Maze, V. Jacques, Competition between electric field and magnetic field noise in the decoherence of a single spin in diamond. *Phys. Rev. B* **93**, 024305 (2016).
27. G. de Lange, Z. H. Wang, D. Ristè, V. V. Dobrovitski, R. Hanson, Universal dynamical decoupling of a single solid-state spin from a spin bath. *Science* **330**, 60–63 (2010).
28. A. Shearrow, G. Koolstra, S. J. Whiteley, N. Earnest, P. S. Barry, F. J. Heremans, D. D. Awschalom, E. Shirokoff, D. I. Schuster, Atomic layer deposition of titanium nitride for quantum circuits. *Appl. Phys. Lett.* **113**, 212601 (2018).
29. K. V. Kepesidis, S. D. Bennett, S. Portolan, M. D. Lukin, P. Rabl, Phonon cooling and lasing with nitrogen-vacancy centers in diamond. *Phys. Rev. B* **88**, 064105 (2013).
30. N. Didier, J. Bourassa, A. Blais, Fast quantum nondemolition readout by parametric modulation of longitudinal qubit-oscillator interaction. *Phys. Rev. Lett.* **115**, 203601 (2015).
31. S. P. Harvey, C. G. L. Bøttcher, L. A. Orona, S. D. Bartlett, A. C. Doherty, A. Yacoby, Coupling two spin qubits with a high-impedance resonator. *Phys. Rev. B* **97**, 235409 (2018).
32. J. Bylander, I. Robert-Philip, I. Abram, Interference and correlation of two independent photons. *Eur. Phys. J. D Atom. Molec. Optic. Plasma Phys.* **22**, 295–301 (2003).
33. S. N. Shevchenko, S. Ashhab, F. Nori, Landau–Zener–Stückelberg interferometry. *Phys. Rep.* **492**, 1–30 (2010).
34. G. Wolfowicz, C. P. Anderson, A. L. Yeats, S. J. Whiteley, J. Niklas, O. G. Poluektov, F. J. Heremans, D. D. Awschalom, Optical charge state control of spin defects in 4H-SiC. *Nat. Commun.* **8**, 1876 (2017).
35. C. M. Wilson, T. Duty, F. Persson, M. Sandberg, G. Johansson, P. Delsing, Coherence times of dressed states of a superconducting qubit under extreme driving. *Phys. Rev. Lett.* **98**, 257003 (2007).
36. G. Thiering, A. Gali, Ab initio calculation of spin-orbit coupling for an NV center in diamond exhibiting dynamic Jahn-Teller effect. *Phys. Rev. B* **96**, 081115 (2017).
37. W. D. Oliver, Y. Yu, J. C. Lee, K. K. Berggren, L. S. Levitov, T. P. Orlando, Mach-Zehnder interferometry in a strongly driven superconducting qubit. *Science* **310**, 1653–1657 (2005).
38. J. R. Maze, A. Gali, E. Togan, Y. Chu, A. Trifonov, E. Kaxiras, M. D. Lukin, Properties of nitrogen-vacancy centers in diamond: The group theoretic approach. *New J. Phys.* **13**, 025025 (2011).
39. R. Brouri, A. Beveratos, J.-P. Poizat, P. Grangier, Photon antibunching in the fluorescence of individual color centers in diamond. *Opt. Lett.* **25**, 1294–1296 (2000).
40. S. J. Balian, G. Wolfowicz, J. J. L. Morton, T. S. Monteiro, Quantum-bath-driven decoherence of mixed spin systems. *Phys. Rev. B* **89**, 045403 (2014).

Acknowledgments: We thank M. Fukami, B. Zhou, F. J. Heremans, V. Dobrovitski, and A. Clerk for helpful discussions and B. Diler for machining assistance. **Funding:** K.C.M., A.B., C.P.A., S.J.W., A.L.C., S.L.B., G.W., and D.D.A. were supported by AFOSR FA9550-14-1-0231 and FA9550-15-1-0029, DARPA D18AC00015KK1932, NSF EFRI EFMA-1641099, and ONR N00014-17-1-3026. G.T., P.U., V.I., and Á.G. were supported by the National Research, Development and Innovation Office in Hungary (NKFIH) grant nos. 2017-1.2.1-NKP2017-00001 (National Quantum Technology Program) and NVKP 16-1-2016-0043 (NVKP Program) as well as grant nos. NN127902 (EU QuantERA Nanospin consortial project) and KKP129866 (Quantum-coherent materials project within National Excellence program) and from the EU Commission (ASTERIQS project with grant no. 820394). V.I. was supported by the MTA Premium Postdoctoral Research Program and the Knut and Alice Wallenberg Foundation through WBSQD2 project (grant no. 2018.0071). H.A. and T.O. were supported by JSPS KAKENHI 17H01056 and 18H03770. This work made use of the Pritzker Nanofabrication Facility of the Institute for Molecular Engineering at the University of Chicago, which receives support from the Soft and Hybrid Nanotechnology Experimental (SHyNE) Resource (NSF ECCS1542205), a node of the NSF's National Nanotechnology Coordinated Infrastructure. **Author contributions:** K.C.M. conceived and demonstrated the optical interference properties with the help of S.J.W., performed VV experiments, and wrote the manuscript. K.C.M., A.B., and A.L.C. developed the scanning confocal microscopy setup. C.P.A. annealed the SiC sample and fabricated planar capacitors and wires on the sample. K.C.M. and S.L.B. performed coherent optical control experiments. G.W. performed cluster-correlation expansion modeling of *kh* VVs. G.T., P.U., V.I., and Á.G. carried out density functional theory calculations of the optical structure and response to electric field perturbation. H.A. and T.O. performed electron irradiation of the SiC samples. D.D.A. advised on all efforts. All authors contributed to the discussions and preparation of the manuscript. **Competing interests:** The authors declare that they have no competing interests. **Data and materials availability:** All data needed to evaluate the conclusions in the paper are present in the paper and/or the Supplementary Materials. Additional data related to this paper may be requested from the authors.

Submitted 15 May 2019
Accepted 24 September 2019
Published 22 November 2019
10.1126/sciadv.aay0527

Citation: K. C. Miao, A. Bourassa, C. P. Anderson, S. J. Whiteley, A. L. Crook, S. L. Bayliss, G. Wolfowicz, G. Thiering, P. Udvarhelyi, V. Ivády, H. Abe, T. Ohshima, Á. Gali, D. D. Awschalom, Electrically driven optical interferometry with spins in silicon carbide. *Sci. Adv.* **5**, eaay0527 (2019).

Science Advances

Electrically driven optical interferometry with spins in silicon carbide

Kevin C. Miao, Alexandre Bourassa, Christopher P. Anderson, Samuel J. Whiteley, Alexander L. Crook, Sam L. Bayliss, Gary Wolfowicz, Gergo Thiering, Péter Udvarhelyi, Viktor Ivády, Hiroshi Abe, Takeshi Ohshima, Ádám Gali and David D. Awschalom

Sci Adv **5** (11), eaay0527.
DOI: 10.1126/sciadv.aay0527